Insights and Challenges of Co-Simulation-based Optimal Pulse Pattern Evaluation for Electric Drives

Lukas Hölsch, Anian Brosch, Richard Steckel, Tristan Braun, Sebastian Wendel, *Member, IEEE*, Joachim Böcker, *Senior Member, IEEE* and Oliver Wallscheid, *Senior Member, IEEE*

***Abstract*—In-depth evaluations of an electric drive's behavior typically result from co-simulation, combining models of motor, power electronics and control software. This approach can be used to evaluate pulse patterns for a given operating point, e.g., for electric vehicle applications, preventing costly real-world experiments. Here, the co-simulation model is fed with offline calculated optimized pulse patterns (OPPs) that are used to increase, among others, the drive's efficiency. Due to the large motor time constant compared to the fundamental wave period, reaching steady state using a simple open-loop control requires unnecessary long simulation times. Hence, a model predictive closed-loop control implementation of the OPPs is proposed which reduced the overall computational effort significantly. However, it turns out that the OPP evaluation using a finite-element-method-based co-simulation for a permanent magnet synchronous motor remains largely uncertain in terms of the predicted power losses which led to the development of a semi-analytical model to further reduce the required computational time. As none of the approaches was able to deliver a suitable trade-off between model accuracy and calculation time, this investigation highlights the remaining challenges of evaluating OPPs based on drive co-simulations motivating further research towards the surrogate-assisted or direct experimental OPP optimization in the future.**

***Index Terms*—Co-simulation, electric drive, inverter, optimized pulse patterns, permanent magnet synchronous motor, semi-analytical model, time domain simulation**

I. Introduction

IMPROVING the operation strategies of electric drives utilizing optimal control techniques is a major challenge in academia and industry. This applies in particular to electric vehicles, where better efficiency brings many advantages. Among others, it reduces the cooling effort of the electric drive, which leads to a lighter and more cost-effective vehicle. The applied pulse patterns have a significant impact on the drives efficiency and overall operation performance, which motivates research toward optimized pulse patterns (OPPs). Considering the complex system dynamics and power loss characteristics of the drive system, a co-simulation coupling the power electronic inverter model, the electric motor model and the control software including the pulse patterns seems to be a particularly interesting evaluation framework for OPPs. This enables relatively detailed loss models behind individual drive components, such as a finite element analysis (FEA) of the electric motor, and to cover the complex loss-related interactions between them [1]. Usually, the operating point of the electric drive is defined by the speed and the required torque, that can be transformed into an average voltage demand for the electric motor which is provided by the modulated voltage source inverter (VSI). The inverter losses are generally rising with an increasing switching frequency and, in comparison to that, the motor losses decrease due to less current distortions. The sum of these two loss curves is the total loss $P_{\mathrm{l,total}}$, whose characteristics are schematically shown in Fig. 1. The goal is to find the loss-optimal pulse pattern for a given operating point, resulting in the highest possible efficiency in that operating point. Thus, one parameter for the optimization is the average switching frequency, which is directly associated to the OPP. The main objective of this research contribution is to investigate the feasibility of an FEA-based co-simulation framework as the basis to evaluate different OPPs and their potential to increase the efficiency of the electric drive for different given operating points beyond the standard approaches such as continuous and discontinuous pulse width modulation (PWM).

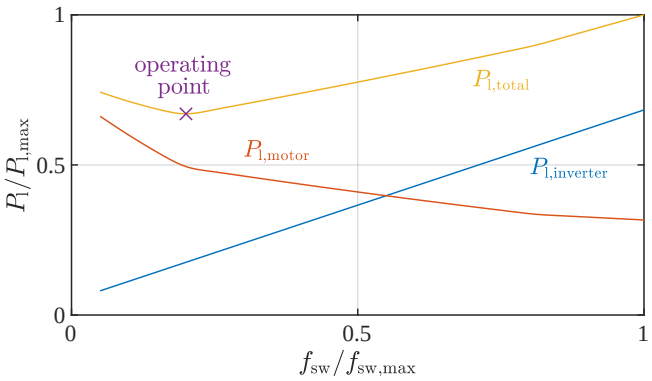

Fig. 1. Exemplary and strongly simplified loss curves illustrating the impact of the average switching frequency on the motor and inverter losses.

A. State of the art

Tab. I contains a literature overview of published FEA-based co-simulation articles with the main key facts. The first finding is, that the general co-simulation approach is not

Manuscript received xx, 202x; revised xx, 202x. (*Corresponding author: Lukas Hölsch.*)

Lukas Hölsch, Anian Brosch, Joachim Böcker and Oliver Wallscheid are with the Department of Power Electronics and Electrical Drives, University of Paderborn, Paderborn 33098, Germany (e-mail: {hoelsch,brosch,boecker,wallscheid}@lea.uni-paderborn.de).

Richard Steckel and Sebastian Wendel are with ZF Friedrichshafen AG, Schweinfurt 97424, Germany (e-mail: {richard.steckel,sebastian.wendel}@zf.com).

Tristan Braun is with ZF Friedrichshafen AG, Friedrichshafen 88046, Germany (e-mail: tristan.braun@zf.com).

TABLE I
LITERATURE OVERVIEW OF FEA-BASED CO-SIMULATIONS FOR ELECTRIC DRIVES

Motor type	Software	Content	Hardware information	Calculation time reported	Ref.
IPMSM	Ansys, MATLAB	- Co-simulation with a closed-loop current control - Comparison between simulated results and experimental measurements	✗	✗	[2]
PMSM	Ansys, MATLAB	- Closed-loop current control - Calculation of eddy currents in segmented magnets with co-simulation	✗	✗	[3]
PMSM	Ansys, MATLAB	- Co-simulation with OPPs and direct MPC closed-loop control - Evaluation of the two control strategies	✗	✗	[4]
PMSM	Ansys, MATLAB	- Detailed description of the co-simulation structure - Closed-loop current control	✓	✓	[5]
DC	Ansys, MATLAB	- General co-simulation setup	✗	✗	[6]
IM	Ansys, MATLAB	- Closed-loop current control - Long calculation time mentioned → development of a lumped-parameter model	✓	✓	[7]
IPMSM	Ansys	- Co-simulation with open-loop applied voltage in Twin Builder - Large time constant of IPMSM visible - Semi-analytical model with flux linkage look-up tables	✗	✗	[8]
PMSM	Altair Flux, Portunus	- Closed-loop current control - Comparison between co-simulation, lumped-parameter model and measurements	✗	✓	[9]
TFM	Altair Flux & Activate	- 3D FEA model - Closed-loop speed control	✓	✓	[10]

limited to a specific motor type. Further, the computing time plays a major role for the FEA-based co-simulation approach. The publications that deal with the computational effort and such that contain any information about the computational hardware are highlighted. Moreover, publications which have identified different challenges in using an FEA-based co-simulation are mentioned, e.g., the open-loop control of a permanent magnet synchronous motor (PMSM). Contrary the optimization or evaluation of different OPPs using an FEA-based co-simulation approach has not been covered in the literature until now.

B. Contribution

This publication describes the challenges of the FEA-based co-simulation approach for evaluating and potentially optimizing offline calculated OPPs. Furthermore, the procedure and challenges to find a loss-optimal pulse pattern for a given operating point are presented. The following points are discussed in detail:

- The influence of the simulation step size in comparison to the OPP resolution and the calculation time;
- The need of a closed-loop control method due to the large time constant of the PMSM;
- Introduction of a closed-loop model predictive control (MPC) algorithm with offline calculated OPPs;
- Discussion of the loss models' accuracy and scope in the context of the given application's background;
- Introduction and comparison against an alternative semi-analytical motor model approach replacing the usual FEA-based motor model within the co-simulation.

II. GENERAL SETUP

In the following, the theoretical basics and the components of the FEA-based co-simulation are described.

A. Coordinate systems

For the transformation between the three-phase abc and the stator fixed $\alpha\beta$ system the matrices in (1) are used. Bold symbols denote matrices and vectors. In this paper † denotes the Moore-Penrose pseudoinverse. The Clarke transformation matrix is given by:

$$\boldsymbol{T}_{\alpha\beta\mathrm{abc}} = \frac{2}{3}\begin{bmatrix} 1 & -\frac{1}{2} & -\frac{1}{2} \\ 0 & \frac{\sqrt{3}}{2} & -\frac{\sqrt{3}}{2} \end{bmatrix}, \boldsymbol{T}_{\mathrm{abc}\alpha\beta} = \boldsymbol{T}_{\alpha\beta\mathrm{abc}}^{\dagger}. \tag{1}$$

Moreover, (2) represents the Park transformation between the stator-fixed $\alpha\beta$ and the rotor-fixed dq coordinate system. Here, $\varepsilon_{\mathrm{el}}$ marks the electrical rotor angle of the PMSM. The transformation can be formulated as follows

$$\boldsymbol{T}_{\mathrm{dq}\alpha\beta}(\varepsilon_{\mathrm{el}}(t)) = \begin{bmatrix} \cos(\varepsilon_{\mathrm{el}}(t)) & \sin(\varepsilon_{\mathrm{el}}(t)) \\ -\sin(\varepsilon_{\mathrm{el}}(t)) & \cos(\varepsilon_{\mathrm{el}}(t)) \end{bmatrix}, \tag{2}$$

with the inverse:

$$\boldsymbol{T}_{\alpha\beta\mathrm{dq}}(\varepsilon_{\mathrm{el}}(t)) = \boldsymbol{T}_{\mathrm{dq}\alpha\beta}^{-1}(\varepsilon_{\mathrm{el}}(t)). \tag{3}$$

The combined transformation between the three-phase abc and the rotor-fixed dq coordinate system can be defined with the following matrices:

$$\begin{aligned} \boldsymbol{T}_{\mathrm{dqabc}}(\varepsilon_{\mathrm{el}}(t)) &= \boldsymbol{T}_{\mathrm{dq}\alpha\beta}(\varepsilon_{\mathrm{el}}(t))\boldsymbol{T}_{\alpha\beta\mathrm{abc}}, \\ \boldsymbol{T}_{\mathrm{abcdq}}(\varepsilon_{\mathrm{el}}(t)) &= \boldsymbol{T}_{\mathrm{dqabc}}^{\dagger}(\varepsilon_{\mathrm{el}}(t)). \end{aligned} \tag{4}$$

B. Motor model

The PMSM is modeled in Ansys Maxwell, which is the used FEA simulation environment. The electric motor is implemented as a 2D model. The reason for that is the dramatically lower computational effort in comparison to a 3D model due to the decreased number of mesh cells. With this reduction in the model complexity comes a certain loss of information. The first one to be mentioned addresses the winding head, which cannot be modelled in a 2D model. Another loss of information is happening when modeling the soft magnetic material. To reduce the eddy current losses, the stator and rotor are manufactured with thin laminations in the axial direction. In the 2D model this lamination can only approximated with a constant factor which decreases the magnetic flux in the axial direction of the motor [11]. Also, permanent magnets are not segmented in the 2D model which prevents detailed insights into the magnet losses, e.g., due to eddy currents. In Fig. 2 an example sketch of a 2D electric motor is presented as utilized by Ansys Maxwell. Due to the rotational symmetry of the motor, only one pole of the PMSM has to be simulated.

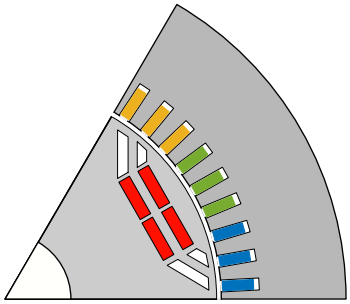

Fig. 2. Exemplary structure of one pole of the PMSM in Ansys Maxwell.

The normalized flux linkage maps can be seen in Fig. 3. These flux linkage maps show the high non-linearity of the magnetic material due to saturation which is typical for electric vehicle applications.

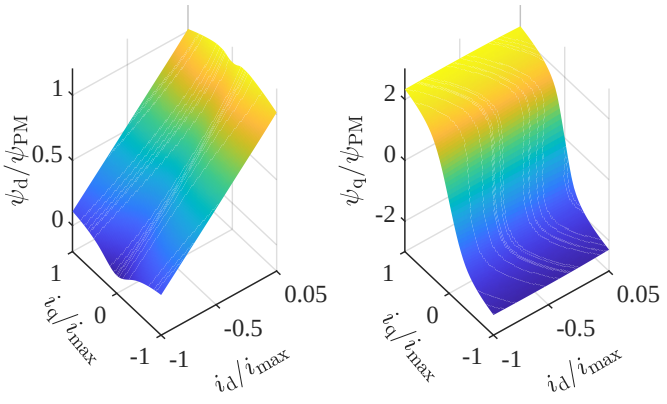

Fig. 3. Flux linkage maps of the utilized PMSM obtained from the FEA simulation.

C. Loss models in Ansys Maxwell

To find the loss-optimal pulse pattern for a given operating point, the motor losses must be calculated. To give a brief overview, the general available loss models in Ansys Maxwell are listed below:

- Power ferrite;
- B-P curve;
- Electrical steel;
- Hysteresis model.

The B-P curve model is used to implement core loss data which are temperature dependent. The power ferrite model represents the losses over different frequencies [11]. For soft magnetic materials in PMSMs, the electrical steel and the hysteresis model are used [11]. The electrical steel model is based on the Bertotti equation [11], which can be described as follows:

$$\begin{aligned} P_{\mathrm{l,fe}} &= P_{\mathrm{h}} + P_{\mathrm{c}} + P_{\mathrm{e}} \\ &= k_{\mathrm{h}} f (B_{\mathrm{m}})^{\beta} + k_{\mathrm{c}} (f B_{\mathrm{m}})^2 + k_{\mathrm{e}} (f B_{\mathrm{m}})^{1.5}. \end{aligned} \tag{5}$$

Here, $P_{\mathrm{l,fe}}$ describes the total iron loss in $\mathrm{W/m^3}$, which is the sum of the hysteresis loss P_{h}, the eddy current loss P_{c} and the excess loss P_{e}. The specific loss factors k_{h}, k_{c} and k_{e} are determined from the corresponding iron loss characteristics. The iron loss is a function of the magnetization frequency f and the magnetic flux density amplitude B_{m}. A more detailed description can be found in [12].

The second model which can be used to calculate the losses for soft magnetic material is the hysteresis model which is based on the Preisach model [13]. This model focuses on the exact replication of the hysteresis curve and has the better accuracy but the calculation effort increases by roughly an order of magnitude as the hysteresis curves are calculated on-the-fly during the simulation, that is, not a simple post-processing as in the Bertotti case [11].

The ohmic winding losses of PMSMs, including skin and proximity losses, are a significant portion of the total losses in the winding head. As mentioned before, the complete winding including the winding head can not be modeled in detail, with the exact geometric dimensions and the resulting eddy current effects, in a 2D model. For a detailed representation of the stator winding losses, a post-processing algorithm outside the Ansys environment is used, which is defined by

$$P_{\mathrm{l,winding}} = \sum_{n=1}^{N} k_{\mathrm{r},n} \;\; R_{\mathrm{DC}} \;\; I_n \tag{6}$$

with the direct current winding resistance R_{DC} and the factor $k_{\mathrm{r,n}}$ that is determined experimentally and describes the raising winding resistance due to the single current harmonics I_n. The current is separated with the Fourier transform for up to N distinct frequencies and added up.

D. Inverter

In this research paper, a two-level three-phase VSI is considered. The average stator voltages are defined as

$$\boldsymbol{u}_{\alpha\beta} \in \mathbb{U}_{\alpha\beta} = \{\boldsymbol{u}_{\alpha\beta} \in \mathbb{R}^2 \mid \boldsymbol{u}_{\alpha\beta} = u_{\mathrm{DC}} \boldsymbol{T}_{\alpha\beta\mathrm{abc}} \boldsymbol{d}_{\mathrm{abc}}\}, \tag{7}$$

with the DC-link voltage u_{DC}. The duty cycle vector is given with:

$$\boldsymbol{d}_{\mathrm{abc}} = \begin{bmatrix} d_{\mathrm{a}} & d_{\mathrm{b}} & d_{\mathrm{c}} \end{bmatrix}^{\top} \in [0,1]^3 \subset \mathbb{R}^3. \tag{8}$$

MOSFETs are used as power semiconductors whose characteristics are presented in Fig. 4. This data is used to calculate the inverter losses which are required to find the loss-optimal pulse pattern for a given operating point. Herein, the switching

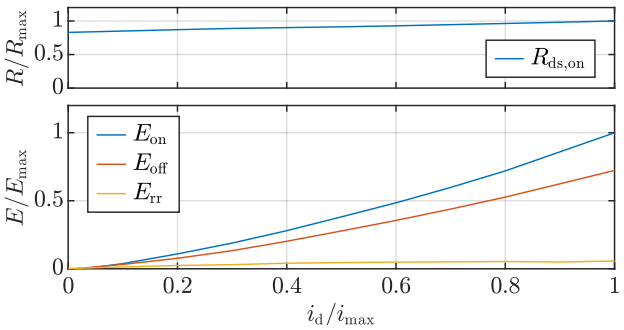

Fig. 4. Normalized drain-source resistance $R_{\mathrm{ds,on}}$ and the normalized switching energies of the considered MOSFET.

energy on (E_{on}) and off (E_{off}) is taken for the loss calculation and, due to the fact of the low value for the reverse recovery energy (E_{rr}), it is neglected. The variable Δs_w classifies switching actions in terms of rising or falling edge of the pulse pattern, which must be determined for each of the $w = 6$ semiconductors:

$$\Delta s_w[k] = \begin{cases} 0 & , s_w[k] = s_w[k-1] \\ 1 & , s_w[k] > s_w[k-1] \\ -1 & , s_w[k] < s_w[k-1] \end{cases}, \tag{9}$$

with discrete time index k and momentary switching state of the semiconductor $s_w[k]$. The switching losses are approximated via

$$P_{\mathrm{l,sw}} = \frac{1}{T_{\mathrm{el}}} \sum_{w=1}^{6} \frac{1}{K} \sum_{k=1}^{K} \begin{cases} 0 & , \Delta s_w[k] = 0 \\ E_{\mathrm{on}}[k] & , \Delta s_w[k] = 1 \\ E_{\mathrm{off}}[k] & , \Delta s_w[k] = -1 \end{cases} \tag{10}$$

for one electrical period T_{el}. The conduction losses $P_{\mathrm{l,cond}}$ are calculated with the following equation

$$P_{\mathrm{l,cond}} = \sum_{x \in \{\mathrm{a,b,c}\}} \frac{1}{K} \sum_{k=1}^{K} R_{\mathrm{ds,on}}(i_x[k]) \; i_x^2[k], \tag{11}$$

where $x \in \{\mathrm{a}, \mathrm{b}, \mathrm{c}\}$ represents the three phases and the drain-source resistance is denoted as $R_{\mathrm{ds,on}}$. In total, the inverter losses are estimated as follows

$$P_{\mathrm{l,inverter}} = P_{\mathrm{l,sw}} + P_{\mathrm{l,cond}}, \tag{12}$$

which can be used to perform the efficiency evaluation of the VSI to evaluate the OPPs.

E. Optimized pulse pattern

In this work, offline OPPs are used, which are a specific kind of a PWM technique [14]. OPPs are part of the synchronized pulse patterns, which means that the start and end pulse of a pulse pattern are synchronized with the motor's fundamental frequency. Compared to other PWM methods, the switching angles are fixed for a certain modulation index m and therefore the switching angles are calculated with a model before starting the application. For this calculation different aspects can be considered. One approach is to eliminate specific harmonics of the electric motor, e.g., the fifth and the seventh harmonics, which is called selective harmonic elimination (SHE). Another optimization approach is to minimize the total harmonic distortion of the motor current. The different optimization methods and objectives are not part of this paper, but the general structure of the OPPs is important. For more details on the OPP derivations, the reader can consult [15].

The OPPs can be categorized into two parts, the symmetrical quarter-wave and the halve-wave pulse pattern with an initial rising or falling edge. This is defined as: $u_{0,\mathrm{pos}} = 1$ and $u_{0,\mathrm{neg}} = -1$. To describe the following setup, the quarter-wave OPP with the initial rising edge is used. An exemplary structure of the pulse pattern with the according mathematical expressions are shown in Fig. 5. The electrical angle $\varepsilon_{\mathrm{el}}$ is located on the horizontal axis. This pulse pattern has only one degree of freedom, which is α_2. If there are more than two switching angles given, the pulse pattern has more degrees of freedom.

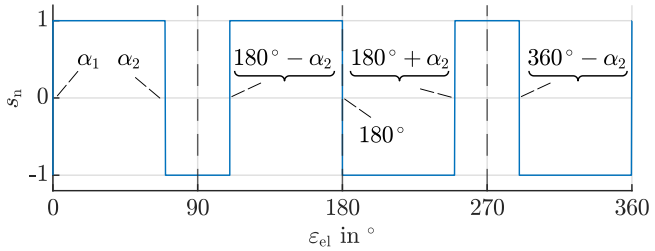

Fig. 5. Exemplary structure of an OPP with one degree of freedom, which is α_2.

In the following, a pulse pattern with more degrees of freedom is analyzed and the corresponding switching angles are shown in Fig. 6. On the horizontal axis, the modulation index m is shown, which means that an individual pulse pattern is assigned to any value of m. At the modulation index around $m \approx 0.8$ there is a discontinuity in the switching angles, which results from the physical basis of the system. The problem of this discontinuity on the control algorithm will be discussed later.

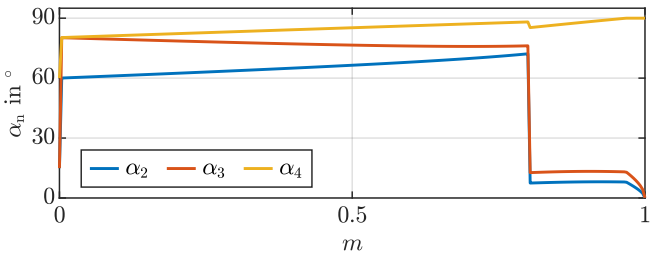

Fig. 6. OPP with three degrees of freedom and one discontinuity at $m \approx 0.8$.

F. FEA-based co-simulation

The general structure and data flow of an FEA-based co-simulation in Ansys with MATLAB Simulink can be seen in Fig. 7 [2]. In MATLAB Simulink the control algorithm of the

PMSM is implemented. The two-level three-phase VSI with the DC-link capacitor is modeled in Ansys Twin Builder. From that, the resulting pulsating voltages $u_{\mathrm{a,b,c}}$ of the inverter are transferred to Ansys Maxwell in which the current and field quantities of the PMSM are calculated with the FEA approach.

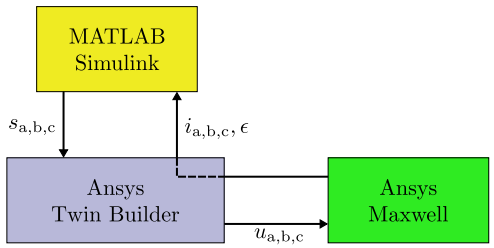

Fig. 7. Structure and data flow of the utilized FEA-based co-simulation setup.

III. Challenges

This section discusses the key challenges in detail, starting with the step size of the FEA-based co-simulation.

A. FEA-based co-simulation step size

The FEA-based co-simulation can only operate correctly with a fixed step size in Simulink and Twin Builder, otherwise some switching pulses might be lost between the two different simulation environments. An adaptive step size, that is, aligning the simulation steps with the switching pulses, is unfortunately not possible due to programming constraints of the used software toolchain, but generally desirable to mitigate the trade-off issue described in the following.

The fixed step size leads to the following challenge between a reference output voltage u^* and the simulated output u. Fig. 8 visualizes one possible signal process, with T_s denoting the step size. After this time has elapsed, the simulated output u is updated. The reference output u^* has a falling edge before T_s ends, resulting in a positive voltage-time error (labeled $+\Delta u$). The same process repeats, but in this case it results in a negative voltage-time error $-\Delta u$. Consequently, the larger the step size, the larger the expected deviation between the reference OPP and the actual simulated OPP is.

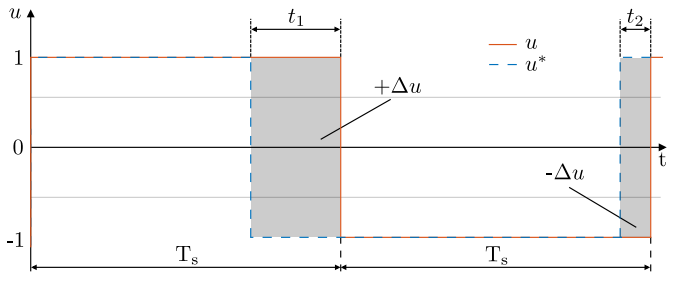

Fig. 8. Simplified sketch to illustrate the problem of a fixed step size. There is a general risk of voltage-time errors between the reference and the simulated inverter voltage output.

Choosing a small step size to mitigate the above-mentioned simulation accuracy issue, however, leads to an increased calculation time effort, that is, a conflicting objective. One possibility to find a good step size compromise is to consider other time constants within the simulation model. Fig. 9 shows the trade-off between the calculation steps per period and the resulting error of the switching angle α. The selected exemplary step size T_s is highlighted by a vertical green line. The figure also shows the time constants for a silicon carbide (SiC) power semiconductor and for an insulated-gate bipolar transistor (IGBT) for illustration purpose. The period duration T_el of the electrical fundamental motor frequency shows the big differences between these values, highlighting the large number of calculations that must be performed to simulate a single electrical period.

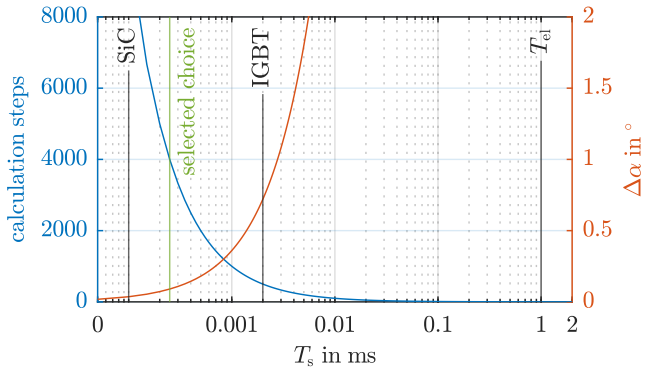

Fig. 9. Number of calculation steps for one electrical period and the resulting error of the switching angle α.

B. Steady-state evaluation of OPPs

The efficiency evaluations of the different OPPs are performed in the steady-state operation. Hence, a rather simple and straightforward approach would be to apply an open-loop control simulation, that is, output a fixed OPP to reach an a priori calculated operating point and wait until the co-simulation model reaches steady state. The advantage of this approach is a shorter developing time due to the simpler implementation. To evaluate this approach, an arbitrary OPP with three switching angles is selected. Fig. 10 shows the trajectories with the transient process for 20 ms. The minimal simulation time to perform the efficiency evaluation, that is, sampling at least one complete fundamental period in steady state, is marked with T_min in the figure. Green background color indicating the steady state.

A reason for the long transient process is the PMSM's stator time constant $\tau = L/R$. To visualize the influence of the inductance on the transient process, the differential equation of the PMSM in the dq coordinate system is given with:

$$\begin{aligned} \boldsymbol{u}_\mathrm{dq} &= R_\mathrm{s}\boldsymbol{i}_\mathrm{dq} + \boldsymbol{L}_\mathrm{dq}(\boldsymbol{i}_\mathrm{dq})\frac{\mathrm{d}}{\mathrm{d}t}\boldsymbol{i}_\mathrm{dq} + \omega_\mathrm{el}\boldsymbol{J}\boldsymbol{\psi}_\mathrm{dq}(\boldsymbol{i}_\mathrm{dq}), \\ \boldsymbol{J} &= \begin{bmatrix} 0 & -1 \\ 1 & 0 \end{bmatrix}, \boldsymbol{L}_\mathrm{dq}(\boldsymbol{i}_\mathrm{dq}) = \begin{bmatrix} L_\mathrm{dd}(\boldsymbol{i}_\mathrm{dq}) & L_\mathrm{dq}(\boldsymbol{i}_\mathrm{dq}) \\ L_\mathrm{qd}(\boldsymbol{i}_\mathrm{dq}) & L_\mathrm{qq}(\boldsymbol{i}_\mathrm{dq}) \end{bmatrix}. \end{aligned} \tag{13}$$

The differential inductances $\boldsymbol{L}_\mathrm{dq}$ for PMSMs are highly non-linear and the values are different in the d and q direction, which is shown in a normalized form in Fig. 11. Due to the

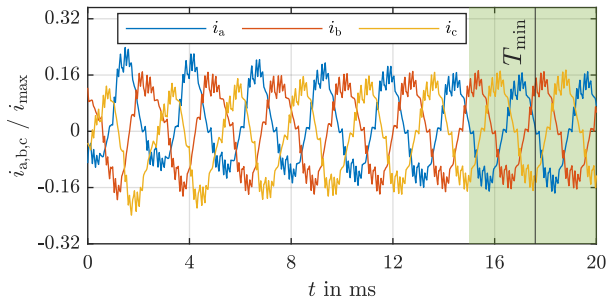

Fig. 10. FEA-based co-simulation with an open-loop control method until steady state is reached, highlighted by green background.

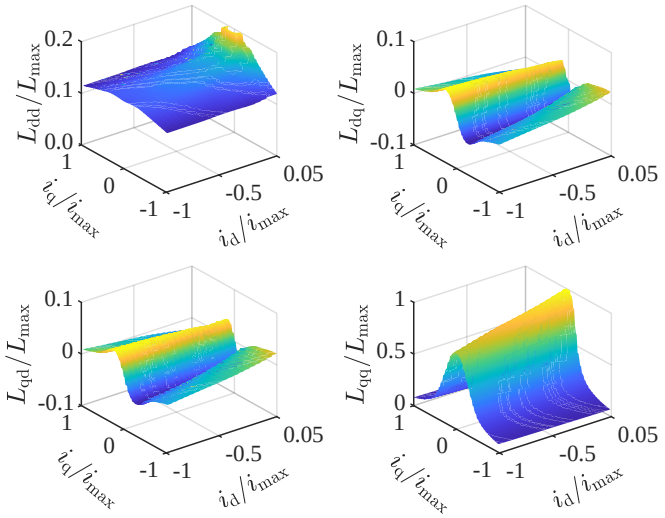

Fig. 11. Differential inductance maps of the utilized PMSM obtained from the FEA simulation with L_{max} is equal to the maximum entry of $\boldsymbol{L}_{dq}$.

normalized values in the figure, in Tab. II the absolute values for some inductances from the literature for PMSMs are given. This table shows that all time constants τ are in the millisecond range, which means that the transient process is always in this time range or worse than in this work as the steady state typically starts after five times the time constant. Consequently, the utilized test motor of this investigation has a stator time constant of roughly 3 ms, which is significantly less than other typical motors in the field and, therefore, the considered simulation time issue for the open-loop OPP approach will be even much more critical for such less dynamic motor designs shown in Tab. II.

For an efficient evaluation of the OPPs, the simulation must reach the steady state as quick as possible to save calculation time. Therefore, a closed-loop control algorithm is presented in the next section.

C. Closed-loop control structure

The next challenge is the implementation of a closed-loop control structure with OPPs. The objective is to control the electric drive as fast as possible towards the steady state such that only a minimum total simulation time must be covered,

TABLE II
TYPICAL PMSM TIME CONSTANTS FROM THE LITERATURE

Author	L	R_s	τ	Reference
Brosch et al.	1.7 mH	18 mΩ	94 ms	[16]
Peña et al.	150 µH	9 mΩ	17 ms	[17]
Hong et al.	0.9 mH	35.9 mΩ	24 ms	[18]
Han et al.	36 mH	34.9 mΩ	103 ms	[19]
Toso et al.	86 mH	1.5 Ω	57 ms	[20]
Ralev et al.	7.25 mH	115 mΩ	63 ms	[21]

that is, to retrieve the co-simulation-based OPP evaluation as fast as possible. The closed-loop control algorithm must also work from the beginning with the OPPs, due to a later change in the control structure results in another transient process. Fig. 12 shows the developed closed-loop control structure. The control algorithm is implemented in MATLAB Simulink, the grey shaded parts are implemented in Ansys.

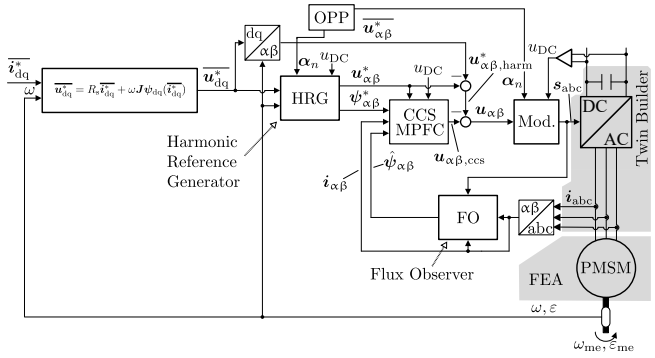

Fig. 12. Implemented model predictive closed-loop control algorithm.

The reference operating point $\overline{\boldsymbol{i}^*_{dq}}$ is given. With the angular speed ω and the motor parameters the reference voltage $\overline{\boldsymbol{u}^*_{dq}}$ is calculated. The harmonic reference generator (HRG) calculates the harmonic reference for the given operating point with the actual OPP. The continuous-control-set model predictive flux control (CCS-MPFC) achieves a high tracking dynamic of the reference flux $\boldsymbol{\psi}^*_{\alpha\beta}$. In the modulation block the modulation index m is calculated with the voltage $\boldsymbol{u}_{\alpha\beta}$ and the corresponding switching angles are read out from the look-up table as it is shown in Fig. 6. With the switching angles $\alpha_{1,\ldots,n}$ the pulse pattern $\boldsymbol{s}_{abc}$ is generated. The flux observer (FO) guarantees an accurate estimation of the flux in $\alpha\beta$ coordinates. A detailed description of the control structure and the HRG can be found in [22].

The performance of the closed-loop control algorithm is shown in Fig. 13. For a better comparability between these two simulation results, the simulation time is set identical to the open-loop control. The steady state, marked with green background color, is reached much faster than with the open-loop control. The closed-loop control simulation reaches the steady state about four times faster, saving a lot of computation time compared to the open-loop control. Here, also the minimal simulation time T_{min} to perform the efficiency evaluation

is marked. This result exhibits the fast transient behavior and the capability of the steady state from the closed-loop control method.

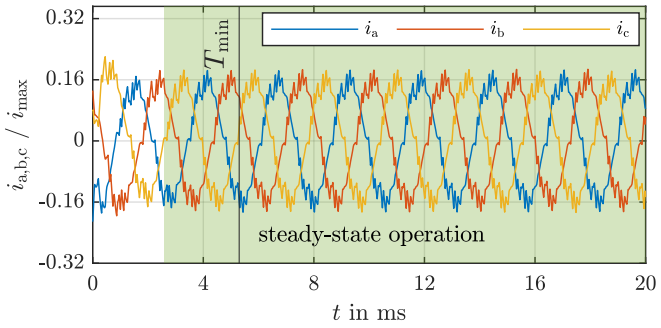

Fig. 13. Transient process and steady state of the closed-loop control algorithm with an FEA-based co-simulation approach.

D. Control impacts of OPP discontinuities

To highlight the challenge with the OPPs discontinuity from the previous section, an example is given. The considered case is a steady-state operating point with a modulation index of $m \approx 0.8$. During the operation, this modulation index varies in time due to some noise in the measurement signals and the high performance of the controller. This is shown in the upper part of Fig.14. The corresponding trajectories of the switching angles α are shown in Fig. 6. If the modulation index is below the threshold value, α will have a high switching angle. Next, the modulation index decreases below the threshold value and the switching angle of α also changes its value below 15 °. This dramatic change of the switching angle causes a complete different pulse pattern as consequence. In combination with the high performance of the controller, this leads to a transient process in the currents and the electric motor no longer operates in steady state. To visualize this problem, the lower part of Fig. 14 shows the trajectory of the switching angle α_1. Several concepts are possible to solve

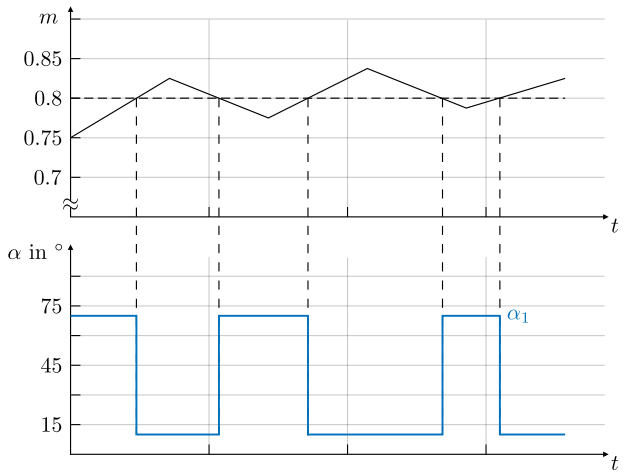

Fig. 14. Simple sketch to highlight the impact of the OPP discontinuity.

this problem. An easy solution could be the introduction of a hysteresis. The idea is that the change in the switching angle only occurs if the modulation index m is significantly higher than the threshold value. An alternative idea is to avoid the OPP discontinuities in the pulse pattern design by introducing continuity constraints.

E. Model uncertainty

In this subsection, the utilized loss models for the FEA calculation are analyzed and discussed. This discussion is done with the aim to evaluate and optimize different pulse patterns for PMSMs, but the following points are generally valid. The loss model accuracy of the electrical steel model is limited. A reason is that this loss model is based on the analytical equation represented in (5). The coefficients of this equation are determined using a curve fitting algorithm [23]. Therefore, this model has good accuracy when the underlying coefficient extraction database matches the same operation range. However, this model is limited due to the fixed number of coefficients and not every trajectory can be well represented. Due to the high non-linearity (Fig. 3) of this type of motor, the predicted losses are uncertain.

Another point for the model uncertainty are minor loops, which are are small hysteresis curves within the main curve and originate from the harmonics caused by the geometry of the motor and by the switching inverter [1], [24]. These minor loops are implicitly considered by the electrical steel model [12], but the hysteresis model implements a more precise approximation. This model generally achieves better accuracy than the electrical steel model, especially when minor loops occur [11]. The hysteresis model explicitly takes the minor loops into account. The disadvantage is the higher computational effort compared to the electrical steel model.

In the actual FEA model, the permanent magnets are modeled in one piece, but often the permanent magnets are segmented in axial direction to reduce torque ripple and eddy current losses [3]. Therefore, an additional approach for a more accurate FEA model is to segment the permanent magnets from the PMSM. However, this is not done because the calculation time increases linearly with the number of segmentations due to a multi-slice approach [11]. Towards a segmentation of n = 5 for a permanent magnet, the calculation time increases with a factor of five [3].

Furthermore, the FEA model can be extended to a complete 3D model. The advantage is, e.g., the possibility to model the PMSM with the winding head. This leads to a better accuracy, e.g., in the calculation of the winding losses compared to the used approach. The disadvantage is a longer calculation time which makes the evaluation of different pulse patterns more complicated.

Consequently, the available motor loss models exhibit significant uncertainties, which makes FEA-based co-simulation efficiency evaluation questionable. Real world experimental results may differ significantly from the co-simulation-based evaluation and optimization values.

F. Calculation time

The keyword calculation time has been used frequently in the literature [5], [7], [9] and [10]. Tab. III visualizes the

calculation time per step within the published articles. To compare these numbers, the table provides information about the selected software and hardware.

TABLE III
COMPARISON OF THE CALCULATION TIME FOR FEA-BASED CO-SIMULATION APPROACHES WITH THE LITERATURE

Software	Hardware information	Calculation time per step	Reference
Ansys	8 GB RAM i7-4710 CPU @2.5 GHz	2.70 s	[5]
Ansys	16 GB RAM i7-6700 CPU @3.4 GHz	0.88 s	[7]
Cedrat Flux	n/a	17.60 s	[9]
Altair Flux	64 GB RAM i7-9700 CPU @3.4 GHz	5.04 s	[10]
Ansys	16 GB RAM AMD Ryzen9 5950X @3.4 GHz	1.36 s	①
Ansys	16 GB RAM AMD Ryzen9 5950X @3.4 GHz	40.40 s	②

The results with the references ① and ② have been produced by the authors of this paper. Most of the calculation times are in the same order, except ②, where a different loss model has been applied. In ①, the electrical steel model is used for the simulation. The hysteresis model is the basis of ②, whose calculation time is around 30 times higher. When the calculation time per step is multiplied by the number of calculation steps per fundamental period from Fig. 9, the real issue of the calculation time becomes visible. An efficiency evaluation for a given operating point takes several hours for the electrical steel model and at least several days with the hysteresis model, which means that an evaluation of many different pulse patterns is not feasible, due to the calculation time. Consequently, FEA-based co-simulated OPP optimization also renders itself infeasible as any optimization algorithm would require many OPP candidate solution evaluations resulting in multi day calculations even on powerful high performance computing clusters. Due to the non-linear drive behavior, the OPPs need to be computed for many separate drive operating points in the speed-torque plane resulting in an unacceptable calculation effort.

IV. CO-SIMULATION WITH SEMI-ANALYTICAL MOTOR MODEL

As the FEA motor model-based co-simulation loss estimates are very uncertain, there is no added value of utilizing this framework to evaluate or even optimize OPPs as any result of doing so would also be uncertain. While utilizing more detailed and accurate FEA-based models within the co-simulation is not a suitable mitigation strategy due to the discussed infeasible computing times, the best alternative is to accept the model-based loss uncertainties while utilizing a computationally more lightweight lumped-parameter motor model approach. This is called the semi-analytical model approach because the analytical first principle equations are the basis of this model. For a more general description, a zero current and flux component is added to the basic equation, which is given by:

$$\boldsymbol{u}_{\mathrm{dq0}} = R_{\mathrm{s}}\boldsymbol{i}_{\mathrm{dq0}} + \frac{\mathrm{d}}{\mathrm{d}t}\boldsymbol{\psi}_{\mathrm{dq0}} + \omega_{\mathrm{r}}\boldsymbol{J}\boldsymbol{\psi}_{\mathrm{dq0}}. \tag{14}$$

Targeting to a more robust numerical implementation, the equation is rearranged such that the flux linkage is based on the left side as follows

$$\boldsymbol{\psi}_{\mathrm{dq0}} = \int_0^t \boldsymbol{u}_{\mathrm{dq0}} - R_{\mathrm{s}}\boldsymbol{i}_{\mathrm{dq0}} - \omega_{\mathrm{r}}\boldsymbol{J}\boldsymbol{\psi}_{\mathrm{dq0}}\mathrm{d}t, \tag{15}$$

where $\boldsymbol{u}_{\mathrm{dq0}}$ is the inverter output and $\boldsymbol{i}_{\mathrm{dq0}}$ is the motor current. At the beginning, the flux linkage vector $\boldsymbol{\psi}_{\mathrm{dq0}}$ is initialized with an according look-up table. Furthermore, the flux linkage maps from Fig. 3 are extended by a zero current i_0 component and the electrical angle $\varepsilon_{\mathrm{el}}$. These flux linkage look-up tables are used to represent the non-linearity due to saturation and the cross-coupling effects on the electric motor model, especially for the PMSM. The aim of this model is to determine the current $\boldsymbol{i}_{\mathrm{dq0}}$ which depends on the flux linkage $\boldsymbol{\psi}_{\mathrm{dq0}}$ in the electric motor. This is done using a look-up table taken from [25] that is defined as follows:

$$\boldsymbol{i}_{\mathrm{dq0}} = \boldsymbol{f}(\psi_{\mathrm{d}}, \psi_{\mathrm{q}}, \psi_0, \varepsilon_{\mathrm{el}}). \tag{16}$$

The transformation matrix between the rotor-fixed dq and the three-phase uvw coordinate systems extends to

$$\boldsymbol{T}_{\mathrm{uvwdq0}} = \begin{bmatrix} \cos(\varepsilon_{\mathrm{el}}) & -\sin(\varepsilon_{\mathrm{el}}) & 1 \\ \cos(\varepsilon_{\mathrm{el}} - \frac{2\pi}{3}) & -\sin(\varepsilon_{\mathrm{el}} - \frac{2\pi}{3}) & 1 \\ \cos(\varepsilon_{\mathrm{el}} - \frac{4\pi}{3}) & -\sin(\varepsilon_{\mathrm{el}} - \frac{4\pi}{3}) & 1 \end{bmatrix}. \tag{17}$$

This approach is used to calculate the motor current $\boldsymbol{i}_{\mathrm{uvw}}$ independently of the motor connection (star or delta), which can be determined by:

$$\boldsymbol{i}_{\mathrm{uvw}} = \boldsymbol{T}_{\mathrm{UVWdq0}}\ \ \boldsymbol{i}_{\mathrm{dq0}}. \tag{18}$$

The model accuracy and the calculation effort of this semi-analytical motor model for a co-simulation approach are discussed in the next section.

V. SIMULATION AND MEASUREMENT RESULTS

In this section, a comparison between the simulation and measurement results is made. The simulations are performed on a workstation (AMD Ryzen 9 5950X @ 3.4 GHz). Tab. IV shows the complete calculation time for one exemplary operating point. The co-simulation with the semi-analytical motor model has a 300 times shorter calculation time than the FEA-based motor model co-simulation approach. Towards a better overview of the different calculation times in this paper and in the literature, the available calculation time reports are visualized in Fig. 15. The model complexity is shown on the horizontal axis which indicates the number of variables determined by the model. In [7] two simulation approaches are presented and both approaches are marked in the figure, [7] represents the FEA-based co-simulation and [7]* marks

TABLE IV
CALCULATION TIME COMPARISON FOR AN OPP CO-SIMULATION WITH TIME LENGTH T = 0.01 S CONSIDERING DIFFERENT MOTOR MODELS.

Simulation method		Time	Step size	Ref.
FEA-based motor model	Electrical steel	909 min	250 ns	①
	Hysteresis model	449 h		②
Semi-analytical motor model		2 min	250 ns	③

the lumped-parameter approach. Concluding, any FEA-based co-simulation requires at least two orders of magnitude more calculation time than a lumped-parameter approach to simulate a given OPP trajectory which highlights the limited usability of FEA-based co-simulations towards large scale OPP evaluation and optimization.

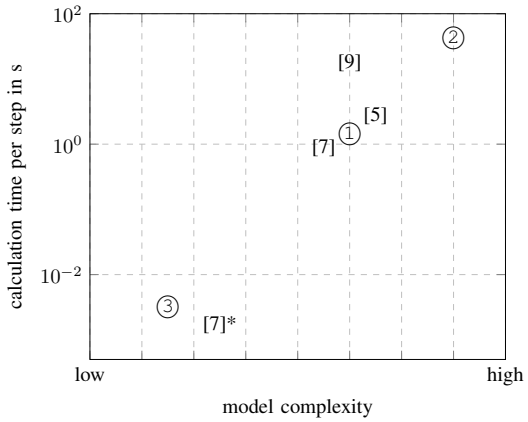

Fig. 15. Visualization of the calculation time per step vs. model complexity of different simulation approaches.

A. Comparison against experimental measurement

Next, the simulations are validated against each other by measurements of a typical PMSM drive for battery electric vehicle on the test bench. The upper part of Fig. 16 shows the phase current i_a of the simulations and the measurement. For a better illustration, only the phase current i_a of each data set is shown, which visualizes small differences in the signal trajectories. The difference between the FEA-based co-simulation model and the measurement is due to an insufficient material model, as described in the previous section. Interpolation errors are the main reason for the difference between the two simulation models. The problem here comes from the generation of the 4D look-up tables, which also includes a comparison between the resolution of, e.g., the electrical angle and the final size of the table. The lower part of the figure shows the PWM signal. In the measurement, several voltage overshoots can be seen, which are absent in the two simulation signals. The reason for this is that the bandwidth of these voltage overshoots is too high for the selected step size in the simulations but not for the test bench measurement equipment.

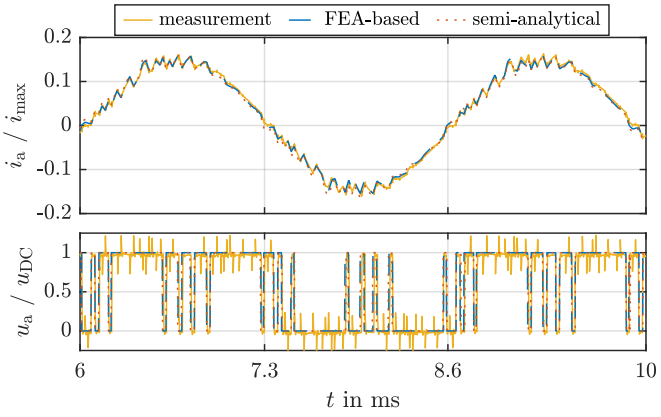

Fig. 16. Evaluation of the two co-simulations considering different motor models with the measurement on the test bench.

To obtain a frequency-oriented view on the current evaluation, the Fourier transform of the signals is investigated. The resulting amplitudes are shown in Fig. 17, where the amplitude of the phase current i_a is shown on the vertical axis. The average switching frequency of the OPPs is around 15 times the fundamental frequency. Both, Fig. 16 and Fig. 17, indicate the high model accuracy regarding the current response prediction of both co-simulation approaches with the FEA-based and the semi-analytical motor model. Moreover, as the PMSM's torque is directly depending on the stator currents, a high prediction accuracy of the torque response can be derived from the experimental comparison shown. Consequently, the much more computationally demanding FEA-based co-simulation does not have a noticeable advantage over the semi-analytical motor model-based co-simulation regarding the transient system response accuracy.

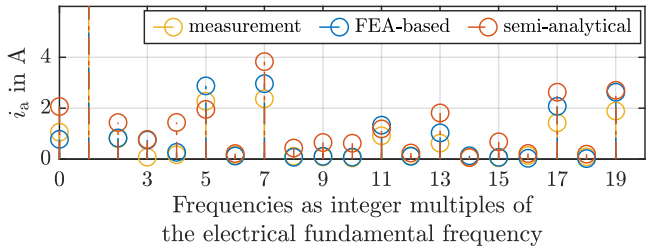

Fig. 17. Visualization of the Fourier components of the phase current i_a from the co-simulations considering different motor models and the measurement for the analyzed operating point n/n_nom = 2.21 and T/T_nom = 0.12.

VI. CONCLUSION AND OUTLOOK

This paper describes the main challenges of designing an FEA-based co-simulation in order to evaluate OPPs for an efficiency maximization of the electric drive. Due to the simulation time demand to cover the entire transient system response given the large stator time constant, an open-loop control is not feasible and a closed-loop control method is developed to save computation time. Based on this co-simulation setup, a discussion of the motor losses points out that the supposedly detailed FEA-based co-simulation is not feasible for evaluating and optimizing different pulse patterns for electric drives, due

to the high uncertainty in the modeling of the losses and herein particularly the iron losses within the electric motor. Another reason is the unacceptable calculation time for the efficiency evaluation of one operating point despite the closed-loop control method of the FEA-based co-simulation that makes an optimization infeasible. The long calculation time and the loss model uncertainty is the reason for developing a semi-analytical motor model as part of the co-simulation that has a 300 times smaller calculation time demand than the FEA-based co-simulation approach. Obviously, the semi-analytical model-based co-simulation does not provide any insight into the motor iron loss behavior, however, that does not represent an important disadvantage over the FEA-based co-simulation given its large loss model uncertainty. It must be concluded that a co-simulation-based evaluation and optimization of OPPs with regard to drive efficiency is not yet possible.

In the light of the identified challenges and limitations of co-simulation-based OPP analysis, future research toward alternative OPP evaluation and optimization approaches that address drive efficiency is motivated. Considering the simulation time issue of the FEA-based co-simulation, data-driven surrogate models could be a potential remedy to enable both, making the simulation results more reliable (e.g., by utilizing a 3D FEA environment to generate a limited set of ground truth data for the surrogate model) and the evaluation toolchain much faster as the surrogate does not require solving the underlying partial differential equations in each time step. Alternatively, a direct experimental evaluation and optimization using highly automated test benches, that is, varying the OPPs in real time and measuring the actual power losses, could be an interesting way of completely circumventing the simulation-to-reality gap.

REFERENCES

[1] S. Steentjes, G. von Pfingsten, M. Hombitzer, and K. Hameyer, "Iron-Loss Model With Consideration of Minor Loops Applied to FE-Simulations of Electrical Machines," *IEEE Trans. on Magn.*, vol. 49, no. 7, pp. 3945–3948, 2013.

[2] C. Schulte and J. Böcker, "Co-Simulation of an Electric Traction Drive," in *Int. Electric Mach. & Drives Conf.*, 2013.

[3] C. Schulte and J. Böcker, "Co-Simulation of an Interior Permanent Magnet Synchronous Motor with Segmented Rotor Structure," in *Annu. Conf. of the IEEE Ind. Electron. Soc.*, 2014.

[4] C. Schulte, K. Peter, M. Leuer, and J. Böcker, "Comparison of Optimized Pulse Patterns with Direct Model Predictive Control Using Co-Simulation," in *IET Int. Conf. on Power Electron., Mach. and Drives*, 2016.

[5] T. K. Mersha and C. Du, "Co-Simulation and Modeling of PMSM Based on Ansys Software and Simulink for EVs," 1, vol. 13, 2022.

[6] A. Rihar, P. Zajec, and D. Vončina, "Cosimulation of Ansys Simplorer and MATLAB/Simulink," in *Int. Conf. on Electr. Drives and Power Electron.*, 2017.

[7] L. Di Leonardo, M. Popescu, M. Tursini, and M. Villani, "Finite Elements Model Co-Simulation of an Induction Motor Drive for Traction Application," in *Conf. of the IEEE Ind. Electron. Soc.*, 2019.

[8] G.-J. Park, H. Jung, Y.-J. Kim, and S.-Y. Jung, "Multi-Domain Co-simulation with Numerically Identified PMSM interworking at HILS for Electric Propulsion," in *Int. Power Electron. Conf.*, 2014.

[9] L. Di Leonardo, F. Parasiliti, M. Tursini, and M. Villani, "Transient Analysis of PM Synchronous Motor Drives by Finite Element Model co-Simulation," in *Conf. of the IEEE Ind. Electron. Soc.*, 2013.

[10] V. Ballestín-Bernad, J. Sergio Artal-Sevil, and J. Antonio Domínguez-Navarro, "Co-Simulation of a Two-Phase Axial-Gap Transverse Flux Machine," in *Int. Conf. on Electr. Mach.*, 2022.

[11] ANSYS, Inc., "Maxwell Help," *ANSYS Electronics Help*, 2021.

[12] D. Lin, P. Zhou, W. Fu, Z. Badics, and Z. Cendes, "A Dynamic Core Loss Model for Soft Ferromagnetic and Power Ferrite Materials in Transient Finite Element Analysis," *IEEE Trans. on Magn.*, vol. 40, no. 2, pp. 1318–1321, 2004.

[13] D. Lin, P. Zhou, C. Lu, N. Chen, and M. Rosu, "Construction of Magnetic Hysteresis Loops and Its Applications in Parameter Identification for Hysteresis Models," in *Int. Conf. on Electr. Mach.*, 2014.

[14] G. S. Buja and G. B. Indri, "Optimal Pulsewidth Modulation for Feeding AC Motors," *IEEE Trans. on Ind. Appl.*, vol. IA-13, no. 1, pp. 38–44, 1977.

[15] A. Birda, J. Reuss, and C. M. Hackl, "Synchronous Optimal Pulsewidth Modulation for Synchronous Machines With Highly Operating Point Dependent Magnetic Anisotropy," *IEEE Trans. on Ind. Electron.*, vol. 68, no. 5, pp. 3760–3769, 2021.

[16] A. Brosch, S. Hanke, O. Wallscheid, and J. Böcker, "Data-Driven Recursive Least Squares Estimation for Model Predictive Current Control of Permanent Magnet Synchronous Motors," *IEEE Trans. on Power Electron.*, vol. 36, no. 2, pp. 2179–2190, 2021.

[17] M. Peña, M. Meyer, O. Wallscheid, and J. Böcker, "Model Predictive Direct Self-Control for Six-Step Operation of Permanent Magnet Synchronous Machines," *IEEE Trans. on Power Electron.*, pp. 1–15, 2023.

[18] G. Hong, T. Wei, and X. Ding, "Multi-Objective Optimal Design of Permanent Magnet Synchronous Motor for High Efficiency and High Dynamic Performance," *IEEE Access*, vol. 6, pp. 23 568–23 581, 2018.

[19] B. Han, J.-S. Lee, Y. Bak, and K.-B. Lee, "Six-step operation strategy for direct self-control method of interior permanent magnet synchronous motors based on torque angle," *J. of Power Electron.*, vol. 21, no. 9, pp. 1352–1364, 2021.

[20] F. Toso, P. G. Carlet, A. Favato, and S. Bolognani, "On-line Continuous Control Set MPC for PMSM drives current loops at high sampling rate using qpOASES," in *IEEE Energy Convers. Congress and Exposition*, 2019, pp. 6615–6620.

[21] I. Ralev, T. Lange, and R. W. De Doncker, "Wide Speed Range Six-Step Mode Operation of IPMSM Drives with Adjustable DC-link Voltage," in *Int. Conf. on Electr. Mach. and Syst.*, 2014.

[22] A. Brosch, O. Wallscheid, and J. Böcker, "Model Predictive Torque Control for Permanent Magnet-Synchronous Motors Using a Stator-Fixed Harmonic Flux Reference Generator in the Entire Modulation Range," *IEEE Trans. on Power Electron.*, vol. 38, no. 4, pp. 4391–4404, 2023.

[23] D. Eggers, S. Steentjes, and K. Hameyer, "Advanced Iron-Loss Estimation for Nonlinear Material Behavior," *IEEE Trans. on Magn.*, vol. 48, no. 11, pp. 3021–3024, 2012.

[24] K. Yamazaki and Y. Takaki, "Iron Loss Analysis of Permanent Magnet Motors by Considering Minor Hysteresis Loops Caused by Inverters," *IEEE Trans. on Magn.*, vol. 55, no. 6, pp. 1–4, 2019.

[25] D. E. Pinto, A.-C. Pop, J. Kempkes, and J. Gyselinck, "dq0-Modeling of Interior Permanent-Magnet Synchronous Machines for High-Fidelity Model Order Reduction," in *Int. Conf. on Optimization of Electr. and Electronic Equipment & Intl Aegean Conf. on Electr. Mach. and Power Electron.*, 2017.